

Article

Computational Approach of Charging and Discharging Phases in a Novel Compact Solar Collector with Integrated Thermal Energy Storage Tank: Study of Different Phase Change Materials

Maria K. Koukou ^{1,*}, Christos Pagkalos ¹, George Dogkas ¹ , Michail Gr. Vrachopoulos ¹, Eleni Douvi ² ,
Yannis G. Caouris ² and Polykarpos Papadopoulos ² 

¹ Energy and Environmental Research Laboratory, General (Core) Department, Psachna Campus, National and Kapodistrian University of Athens, 34400 Evia, Greece; pagkalos.christos@gmail.com (C.P.); geodogas@mail.ntua.gr (G.D.); mgrvrachop@uoa.gr (M.G.V.)

² Department of Mechanical Engineering & Aeronautics, University of Patras, 26504 Rio Achaia, Greece; douvi.eleni@gmail.com (E.D.); caouris@upatras.gr (Y.G.C.); p.papadopoulos@des.upatras.gr (P.P.)

* Correspondence: mkoukou@uoa.gr

Abstract: A numerical study was carried out to investigate charging and discharging processes of different phase change materials (PCMs) used for thermal storage in an innovative solar collector, targeting domestic hot water (DHW) requirements. The aim was to study PCMs that meet all application requirements, considering their thermal performance in terms of stored and retrieved energy, outlet temperatures, and water flow rate. Work was carried out for three flat-plate solar panels of different sizes. For each panel, a PCM tank with a heat exchanger was attached on the back plate. Simulations were conducted on a 2D domain using the enthalpy–porosity technique. Three paraffin-based PCMs were studied, two (A53, P53) with phase-change temperatures of approximately 53 °C and one of approximately 58 °C (A58H). Results showed that, during charging, A58H can store the most energy and A53 the least (12.30 kWh and 10.54 kWh, respectively, for the biggest unit). However, the biggest unit, A58H, takes the most time to be fully charged, i.e., 6.43 h for the fastest feed rate, while the A53 unit charges the fastest, at 4.25 h. The behavior of P53 lies in between A53 and A58H, considering stored energy and charging time. During discharging, all PCMs could provide an adequate DHW amount, even in the worst case, that is, a small unit with a high hot water consumption rate. The A58H unit provides hot water above 40 °C for 10 min, P53 for 11 min, and A53 for 12 min. The DHW production duration increased if a bigger unit was used or if the consumption rate was lower.

Keywords: domestic hot water; heat exchanger; latent heat storage; paraffin; PCM; simulation; solar collector



Citation: Koukou, M.K.; Pagkalos, C.; Dogkas, G.; Vrachopoulos, M.G.; Douvi, E.; Caouris, Y.G.; Papadopoulos, P. Computational Approach of Charging and Discharging Phases in a Novel Compact Solar Collector with Integrated Thermal Energy Storage Tank: Study of Different Phase Change Materials. *Energies* **2022**, *15*, 1113. <https://doi.org/10.3390/en15031113>

Academic Editor: Luisa F. Cabeza

Received: 11 December 2021

Accepted: 27 January 2022

Published: 2 February 2022

Publisher's Note: MDPI stays neutral with regard to jurisdictional claims in published maps and institutional affiliations.



Copyright: © 2022 by the authors. Licensee MDPI, Basel, Switzerland. This article is an open access article distributed under the terms and conditions of the Creative Commons Attribution (CC BY) license (<https://creativecommons.org/licenses/by/4.0/>).

1. Introduction

Fossil fuel depletion and environmental pollution have shifted the production of energy towards renewable energy sources (RES). The latter are constantly replenished according to the cycle of nature and are considered as practically inexhaustible. One of the most commonly used RES is solar energy. It is one of the cleanest and most abundant RES and can be easily converted into thermal or electrical energy. The main issue with solar energy is the gap between energy production and energy demand, together with the efficiency of the solar collectors, so it is important for such systems to find ways to improve their performance. A promising technology to improve performance is to incorporate energy storage technologies and materials.

Phase change materials (PCMs) utilize latent heat thermal energy storage (LHTES), a mechanism for storing energy when they change their phase. Due to their high energy densities, they are ideal for storing energy in small volumes. PCMs, as might be expected,

change their phase with an input of heat at a specific temperature or narrow temperature range, and release this energy later when it is needed. In comparison to the storage of sensible heat, there is almost no temperature difference during the most productive part of the storage process [1,2]. There are a significant number of published materials on latent heat storage. Overviews of the materials and their properties were conducted by, among others, Elias and Stathopoulos [3] and Demirbas [4]. The LHTES units using PCM that alter from the liquid to the solid phase are widely used in feasible applications [5–10]. Liquid–solid phase change does not yield any mechanical stresses on the parts of the assembly, like those resulting from a gas–liquid phase change material. Another interesting characteristic of the LHTES units is their capacity to store energy in a limited temperature range (around the phase-change temperature), providing a design that achieves optimum operation.

In recent years it has been shown that latent heat storage is the best solution for increasing efficiency, due to its compact nature and high energy density [11–13]. Systems that use encapsulated PCM in the existing water tank can improve heat transfer due to the high surface-area-to-volume ratio and cycling stability. In solar DHW systems, the PCMs can be integrated either into the storage tank or directly to the solar collector, or they can be handled as separate PCM units in the hot water closed circuit [14]. The storage tank with integrated PCM is the most frequently used method and has been extensively studied to date, both experimentally and theoretically [8], [15–19]. Some of those studies are concentrated on the application of different PCMs [16,17], while others are concentrated on the storage tank [18,19]. The integration of PCM into the solar collector can be under the absorber plate of the collector, concentrically to the flow line [20] or as a separate thermal energy storage unit [15,16], [21]. However, the most compact configuration for a flat-plate collector is to put the thermal storage tank under the absorber plate.

The thermal conductivity of most PCMs is particularly low, resulting in low charging–discharging rates; thus, techniques to improve heat transfer are required for most latent-heat storage applications. One technique that has been studied more extensively, both experimentally and computationally, is the enhancement of heat transfer by means of finned heat exchangers of different configurations [22,23]. I. Khan and M. Khan have experimentally investigated a solar thermal storage unit with a shell-and-tube heat exchanger, with or without longitudinal fins. They concluded that the charging or discharging duration is significantly shorter with the fin configuration [24]. Another technique that has been extensively studied is the addition of high-conductivity (nanoparticles) particles to the PCM [25,26], which is not commercially common at this time, so the cost of this technique is higher than conventional solutions such as finned heat exchangers.

Naghavi et al. [27] carried out an experimental study of a solar DHW system with evacuated tubes integrated with a 57 kg paraffin PCM tank, having a melting-point range of 53–57 °C. The unit did not have a water tank for storing hot water and it could produce 56–85 L of hot water for every 1 m² of solar collector area, operating at the worst conditions possible. They also found that the thermal energy stored in the PCM did not suffer from large losses during the night because of the low thermal conductivity of the PCM. Kilickap et al. designed a hot water tank with an outer shell of PCM, directly coupled on top of a conventional flat-plate solar collector [28]. The melting point range of the PCM was 28–35 °C. The maximum water temperature inside the water tank was found to be 89 °C and the collector efficiency (defined as the ratio of solar energy collected in the heat transfer fluid (HTF) to the solar radiation intercepted by the collector) was calculated up to 58%. Moreover, Fadl and Eames built a PCM storage tank filled with 37.8 kg of PCM using a 27 m long copper tube [29]. The tube was fed with water at a constant temperature at various flow rates, simulating the charging and discharging process of an LHTES system that provides DHW. For charging, 70, 75, and 80 °C of inlet water temperatures were tested at volume flow rates equal to 2, 4, and 6 L·min^{−1}, while for discharging, the water inlet temperature was constant (40 °C) and the examined flow rates were 1.7, 2.3, and 5.1 L·min^{−1}. The stored energy during charging was calculated as being equal to 2.85 kWh, a value matching the theoretical capacity. The duration ranged between 184 and 219 min, depending on the

flow rate. The authors concluded that the impact of the HTF inlet temperature was greater than the impact of the flow rate on the process. During discharging, the retrieved energy absorbed by the HTF ranged between 2.27 and 2.67 kWh, depending on the flow rate.

This study examined a novel solar energy thermal storage system named Solar Kit, which utilizes solar energy in order to provide DHW. It is a compact solution that consists of a commercial flat-plate solar collector and a thermal energy storage tank that contains a high efficiency heat exchanger (HE) immersed into the PCM. The finned-tube HE compensates for the low thermal conductivity of organic PCMs and can perform at high heat-transfer rates.. Due to PCMs' high energy density, it is targeted to decrease the required volume and respectively the available area required, which is very important when considering the limited existing available spaces in buildings. The compact shape of the design, due to the use of the integrated PCM, provides an effective and easy-to-install system that requires the minimum length of piping. The work was implemented through a direct collaboration with the solar collector manufacturer DIMAS SA [30]. The company provided three differently sized solar panels of its products for the development of the novel Solar Kit collector. The HE immersed in the PCM was connected to the solar collector in a closed circuit of water circulation, in order to store heat by melting the PCM. Design considerations comprise the type of HE, the sizing of all equipment, and the selection of the PCM and all auxiliary devices. The size of the HE and of the storage tank were dictated by the size of the solar collectors. One of the issues that should be taken into account when developing a cost-effective thermal energy storage solution is the PCM selection. In this way, the study of the different PCMs contributed to the design of the system, as it assisted in understanding the phenomena taking place in the innovative collector when using them. The PCMs studied were all organic and, therefore, chemically stable, they do not suffer phase separation, they are nontoxic, and they are not corrosive to metals such as salt hydrates.

A numerical study was performed to investigate the charging and discharging phases of three commercial PCMs, and typical results are presented and discussed in this study. For the charging process, the device must be able to harvest and store all of the available solar thermal energy and also accomplish full melting. In addition, the collector must operate at such conditions that maximize its efficiency. Furthermore, for the discharging process, higher heat transfer rate is needed to quickly heat the water delivered for consumption at the bath tap. Therefore, the different requirements for charging and discharging operations must be investigated. Moreover, in this study, different PCMs that met all Solar Kit requirements were studied, so as to select the one with sufficient thermal performance at a low cost. Furthermore, the Solar Kit performance according to parameters such as the proper flow rate conditions and the solar collector area were also studied. Three different Solar Kit units were considered for simulations, based on the commercial solar collector's gross area, as indicated by the manufacturer DIMAS SA [30].

2. The Solar Kit Apparatus

Solar Kit consists of a commercial flat solar panel and a flat tank filled with PCM, which is attached directly behind the solar collector, as shown in Figure 1. The HTF is heated by the absorbed solar energy and circulates in a closed loop, from the solar collector to the tank, transferring heat to the PCM via a heat exchanger mounted inside the tank. Subsequently, the PCM starts melting (charging phase), thus storing energy due to latent heat. The storage tank HE is finned for enhanced heat transfer performance, while the whole system is insulated to reduce heat losses to ambient.

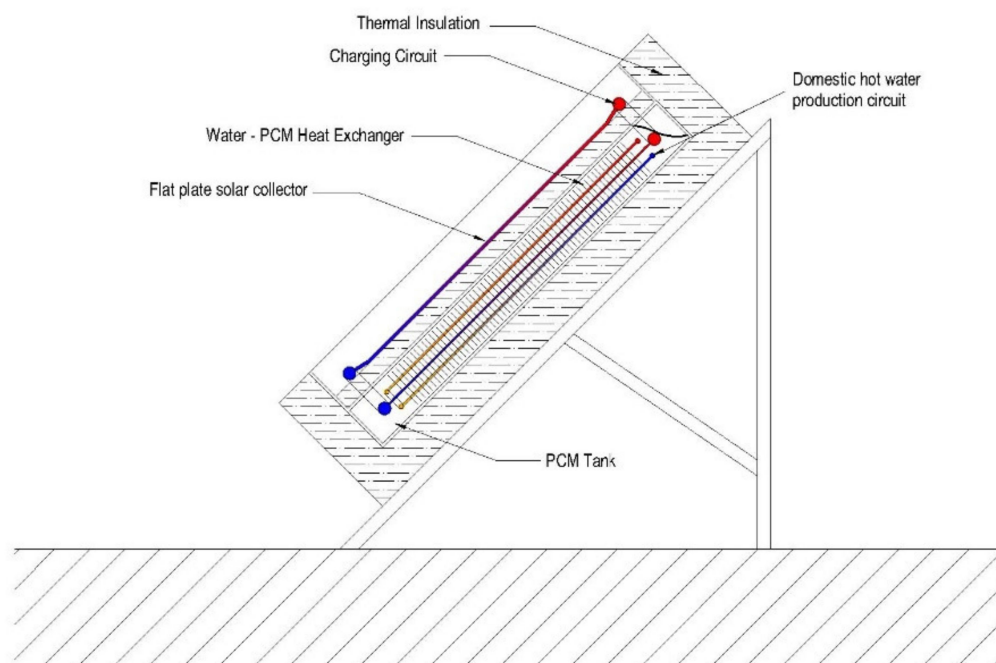


Figure 1. View of Solar Kit collector (cross section).

When hot water is needed for consumption, cold water from the city mains enters the open circuit of the heat exchanger, absorbing heat from the hot PCM (discharging phase), exiting the tank ready for use. After this process ends, the PCM returns to the solid phase and the charging process is ready to start again.

The selected HE type for the Solar Kit project is a commercial one, widely used in air conditioning units, with aluminum fins and copper tubes. Its efficiency and power density are much higher than those of other similar types of HEs and it is ideal for thermal energy storage applications [8,31–34]. Based on efficiency measurements and estimates of the time required for complete melting of the PCMs, it has been proven that this type of HE has a high average thermal power and a high ratio of heat transfer. Working closely with the solar panel manufacturer Dimas SA [30], three different-sized collectors were selected to be studied. The collector selected is a flat plate-type, glazed solar collector available in panels of various sizes. Each panel has individual dimensions providing different absorbing areas. Technical information and layouts of the solar collectors are shown in Table 1 and Figure 2.

Table 1. Solar collector geometrical details [29].

Collector Name	Gross Area m ²	Absorbing Surface m ²	Gross Length mm	Gross Width mm	Gross Height mm
HE1—Small (Terra+Evo15)	1.51	1.35	1503	1007	103
HE2—Medium (Terra+Evo20)	2.02	1.83	2006	1007	103
HE3—Big (Terra+Evo29)	2.92	2.71	2006	1457	103

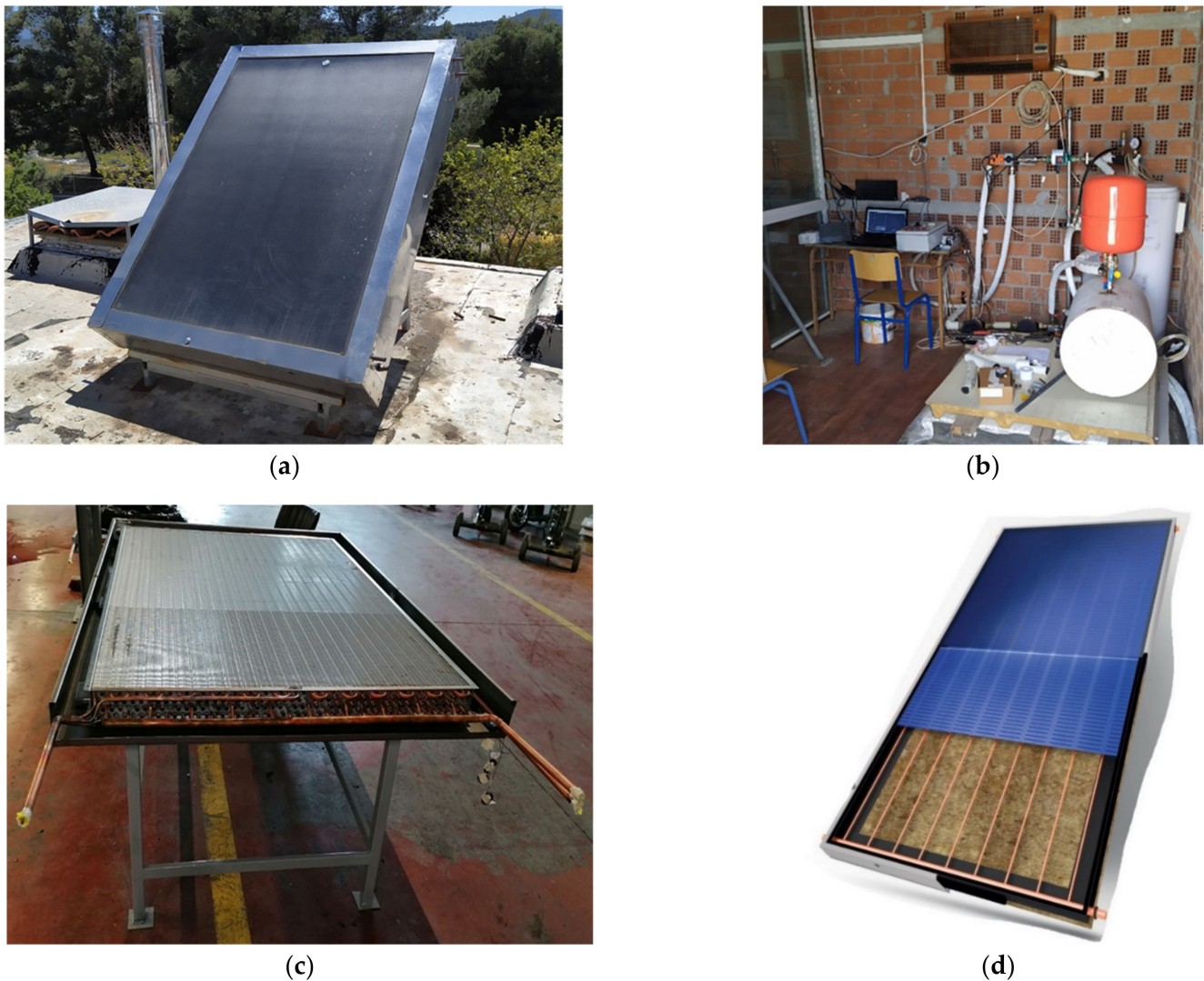


Figure 2. Pictures of the experimental rig of the Solar Kit apparatus: (a) the Solar Kit unit; (b) data acquisition and control; (c) heat exchanger; and (d) solar collector.

The dimensions of the studied HEs are selected to match with the dimensions of the respective solar panels, which have an area of $\sim 1.5 \text{ m}^2$, 2.0 m^2 , and 2.9 m^2 for the small, medium, and large respectively. At each panel, a tank containing the PCM and the heat exchanger is attached on the back. Each HE has different circuits for charging and discharging the PCM. In the closed charging circuit, the HTF (water) circulates between the solar collector and the tank to heat the PCM. In the open discharging circuits, water enters at the main's supply temperature, is heated, and exits for consumption. An image of the HE is presented in Figure 2c and details of the HEs' geometry are given in Table 2.

The charging circuits comprise parallel tubes that drive the HTF through a manifold to the PCM to melt it and return to a second manifold for recirculation in the closed circuit. For each solar panel/HE, the HE tubes configuration are as follows:

- Small size solar collector: the HE has 14 parallel tubes with a length of 1.24 m each.
- Medium size solar collector: the HE has 14 parallel tubes with a length of 1.75 m each.
- Large size solar collector: the HE has 20 parallel tubes, with a length of 1.75 m each, resembling the medium-size configuration.

The discharging circuits have the following arrangements:

- Small size solar collector: the HE has two circuits with a length of 23.5 m each.
- Medium size solar collector: the HE has two circuits with a length of 26.25 m each.

- Large size solar collector: the HE has four circuits with a length of 22.75 m each.

Table 2. Geometrical details of the HEs—Charging and Discharging circuits.

		Heat Exchanger 1 (HE1)	Heat Exchanger 2 (HE2)	Heat Exchanger 3 (HE3)
Heat exchanger Dimensions	Length (m)	Charging: 1.24 Discharging: 23.50	Charging: 1.75 Discharging: 26.25	Charging: 1.75 Discharging: 22.75
	Width (m)	0.80	0.80	1.25
	Height (m)		0.0866	
Number of charging tubes		Charging: 14 Discharging: 2	Charging: 14 Discharging: 2	Charging: 20 Discharging: 4
Outer Tube Diameter (mm)		9.525		
Tube Thickness (mm)		0.8		
Fin spacing (mm)		0.005		
Number of fins		Charging: 234 Discharging: 4292	Charging: 330 Discharging: 4952	Charging: 330 Discharging: 4433
Fin Dimensions	Thickness (m)	0.0003		
	Length (m)	0.80	0.80	1.25
	Height (m)	0.0866		

3. Computational Approach

The charging and discharging processes in the thermal storage tank were studied by applying numerical simulation using the commercial computational fluid dynamics (CFD) code ANSYS® Fluent 18.1 [34]. The key parameters that affect the operation and performance of the system for both charging and discharging were investigated. These are the geometric characteristics of the HE, the PCM to be used, and the HTF mass flow rate. The model utilizes the enthalpy–porosity method to simulate the phase change process [34] and more details are given in the Appendix A.

Three different organic PCMs, with melting temperatures and latent heat values suitable for the DHW application, were computationally studied. The selected PCMs were chemically stable and compatible with the Solar Kit collector materials. For each PCM, three different tube lengths were studied, representing the three different HEs, and for each tube length, three different indicative flow rates were applied. The discharging process was simulated mainly for worst-case scenarios, by applying the lowest inlet temperature for water from the city supply network, and high flow rate. If the system performs adequately under these circumstances, it can be safely assumed that it can provide the required water under normal conditions.

During the implementation of the computational approach, two assumptions were made, in addition to that of the 2D domain. The PCM density was considered constant, and no thermal losses were taken into account. Additionally, the physical behavior of PCMs is not straightforward, but it changes with their mass or heating rate. It is known that the phase change properties of PCMs are different during differential scanning calorimetry measurements and when the quantity is more than a few milligrams [35]. Furthermore, the rate at which the PCM is heated (or cooled), also affects its physical properties [36,37]. This behavior of the material cannot feasibly be described exactly by a computational model. In addition, the volume taken into consideration in the simulation consists of the active PCM volume. The active PCM volume is considered as the volume of PCM in direct contact with the HE. Inside the thermal storage tank, the HE is immersed in the PCM where most of it lies between the fins and the tubes of the HE. Moreover, due to the low thermal conductivity of the PCM under extreme conditions (winter, low sunlight, etc.), in areas inside the tank away from the HE, PCM does not fully melt during the charging process. The active volume approach was selected, as it can be assumed that all the PCM considered has melted. For each of the charging and discharging tubes, the amount of

PCM in the vicinity of the fins and tubes was calculated, and the same amount was used in each simulation.

3.1. Geometry and Computational Grid Development

The geometry used for the simulation was a simplified model for each HE. For each tube of the HE, for both charging and discharging circuits, the corresponding volume was calculated and inserted into the simulations. A 2D axisymmetric geometry was used, with the aim of saving computational resources and reducing the computational time. This approach is highly recommended for symmetrical flow regimes around an axis, such as the computational domain of the HE around the pipe centerline. The entire area of the experimental apparatus rectangular fins was in direct contact with the PCM and such was the case of the circular CFD fins. The geometrical domain used in the simulations represented the original HE dimensions; it was not scaled down, and shown in Figure 3.

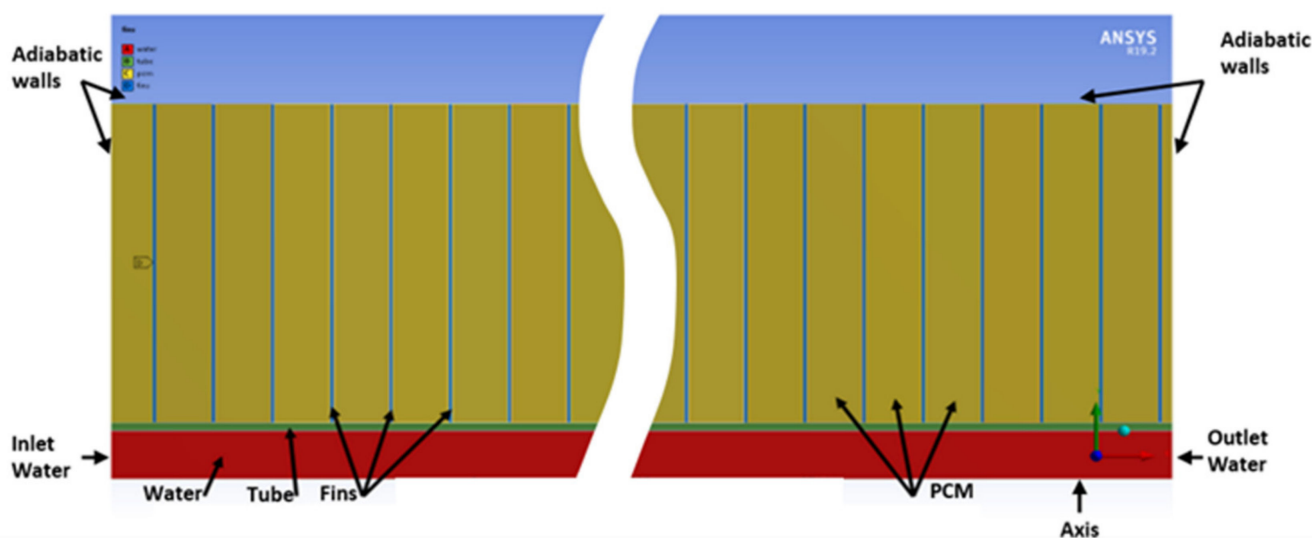


Figure 3. Heat exchanger 2D geometry—water (red), tube (green), fins (blue), PCM (olive green).

For the charging and discharging processes, only one of the charging/discharging tubes was simulated. Due to the distance between the tubes in the HE, the effect of the neighboring charging tubes was not calculated, as it was expected to be rather insignificant. This effect would be beneficial to the charging process, and by omitting it, it was ensured that the system could work even in the worst conditions. Details for the geometry used in the computational model are given in Tables 3 and 4.

Table 3. Geometrical features of the computational model for the HE-charging process.

	Heat Exchanger 1	Heat Exchanger 2	Heat Exchanger 3
Fin Height (m)	0.0314	0.0314	0.0334
Active PCM Volume (per tube) (m ³)	0.0049	0.0069	0.0077

Table 4. Geometrical features of the computational model for the HE-discharging process.

	Heat Exchanger 1	Heat Exchanger 2	Heat Exchanger 3
Fin Height (m)	0.023	0.025	0.024
Active PCM Volume (m ³)	0.0704	0.0993	0.1547

The discharging circuit differs from that of charging, as the latter consists of several tubes connected in parallel, while the discharging circuit comprises a single tube, traversing the HE. The length of the discharge tube is multiple times greater than the length of the charging tube, as shown in Table 2, where geometrical details for the three HEs are presented for the discharging process.

A mesh independence study was conducted for the three (3) different HEs studied. For the small HE (HE1), five different meshes were generated with an element size equal to 0.5 mm, 0.45 mm, 0.4 mm, 0.3 mm, and 0.2 mm, which resulted in 193050, 232981, 304575, 522164, and 1118109 elements, respectively.

In the following figures, the results of the mesh independence study are shown. In Figure 4, the average PCM temperature (a) and the average water temperature at the outlet (b) for the different meshes are presented. As can be seen from both diagrams for the two most populated meshes, the results have become almost equal.

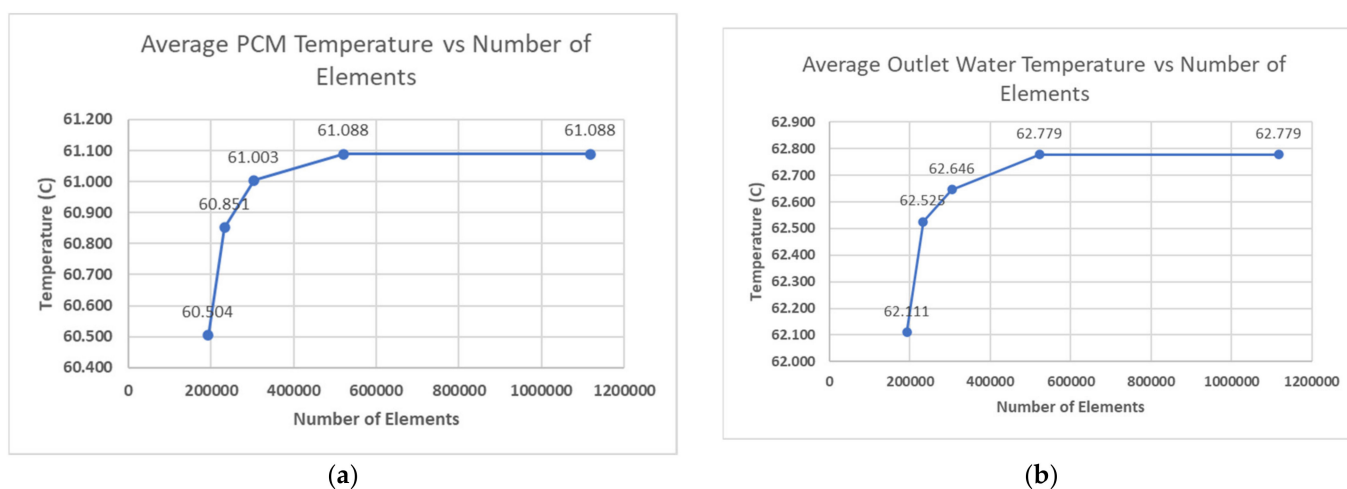


Figure 4. Mesh independence study, (a) average PCM temperature; and (b) average water temperature versus number of elements used in the computational grid.

In addition, the computational time required for the full melting of the PCM was monitored for each mesh size. The computational time needed for the simulation was 5.2 h for the mesh with the fewest elements, and 7.6 h for the mesh with the most elements. For the selected mesh, the simulation lasted for about 6.8 h. As was expected, the difference in the computational time between the most accurate meshes was obvious.

Given the outcomes of the mesh independence study, the mesh comprising 522164 elements (0.3 mm element size) was selected for the simulations. For the other two HEs and for the discharging HEs, the same procedure was followed in order to generate a valid mesh. The mesh size for the geometries used for each HE is shown in Table 5. A full view of the computational mesh for HE1 of the charging process is given in Figure 5a and an enlarged view in Figure 5b.

Table 5. Mesh size for the geometries used.

	Heat Exchanger 1	Heat Exchanger 2	Heat Exchanger 3
Number of Elements	Charging circuit	522.164	778.533
	Discharging circuit	6.145.293	5.949.174

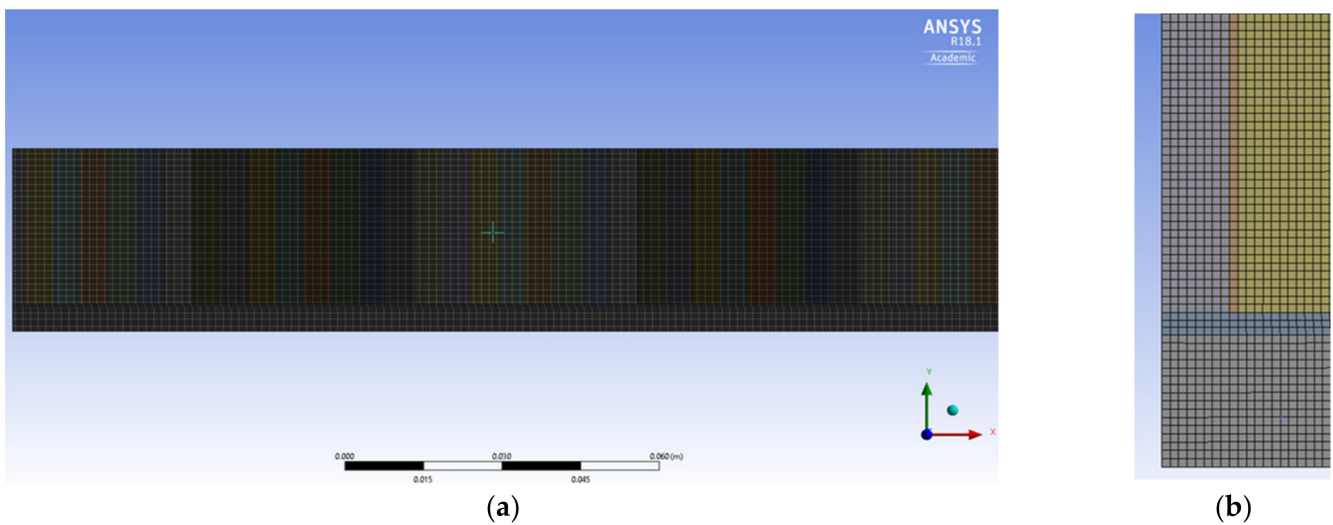


Figure 5. (a) Computational mesh of HE1 for charging; (b) enlarged view of the mesh.

3.2. PCM Properties

The PCMs studied were chosen based on the requirements of the Solar Kit application that targets DHW production. Three paraffin-based materials were studied: A53, A58H, and P53. The number in the name of the PCMs designates the nominal temperature at which the material changes phase. The phase change temperature for A53 and P53 is about 53 °C, while for A58H, it is about 58 °C. A53 and A58H are commercially available PCMs, provided by PCM Products Ltd. [38], while P53 is a pure paraffin, called Paraffin 53, provided by a local supplier in Greece. The properties of A53 and A58H were provided by the manufacturer, while for P53 they were determined, after a series of measurements, in the Energy and Environmental Research Laboratory of the National and Kapodistrian University of Athens, and in collaboration with the University of Ioannina. Mean values and errors were estimated from measurements of 27 independent samples, based on the applied method from Evangelakis et al. [39]. The error in the calculation of thermal conductivities is $\pm 0.02 \text{ W}\cdot\text{m}^{-1}\cdot\text{K}^{-1}$, for specific heat $\pm 0.01 \text{ kJ}\cdot\text{kg}^{-1}\cdot\text{K}^{-1}$ and for latent heat $\pm 8 \text{ kJ}\cdot\text{kg}^{-1}$. The cost of P53 is significantly lower in comparison with the costs of A53 and A58H. The properties of the PCMs are presented in Table 6.

Table 6. PCM properties.

		A53 [37]	A58H [37]	P53
Density ($\text{kg}\cdot\text{m}^{-3}$)	Solid	839	816	901
	Liquid	772	790	776
Thermal Conductivity ($\text{W}\cdot\text{m}^{-1}\cdot\text{K}^{-1}$)		0.22	0.22	0.37
Specific Heat ($\text{J}\cdot\text{kg}^{-1}\cdot\text{K}^{-1}$)	Solid	2400	2400	2700
	Liquid	1800	1800	2600
Latent Heat ($\text{J}\cdot\text{kg}^{-1}$)		237,000	284,000	240,000
Viscosity ($\text{kg}\cdot\text{m}^{-1}\cdot\text{s}^{-1}$)			0.007	
T_{solidus} (K)		324.20	329.00	328.15
T_{liquidus} (K)		325.60	330.40	331.15

3.3. Model Validation

In order to validate the CFD model and to examine whether it was appropriate for the parametric study, the computational results were compared with the corresponding

experimental data received from testing the first approach of the Solar Kit unit. The comparison was made for HE1 with P53 during charging with the highest HTF flow rate. The experimental rig consisted of the solar collector coupled with the insulated PCM tank, all the necessary auxiliary hydraulic equipment, as well as measuring equipment. The experimental rig is depicted in Figure 2 and data from a day of August 2020 are used for comparison with the CFD results. The computational results and the experimental data of water temperature are presented in Figure 6.

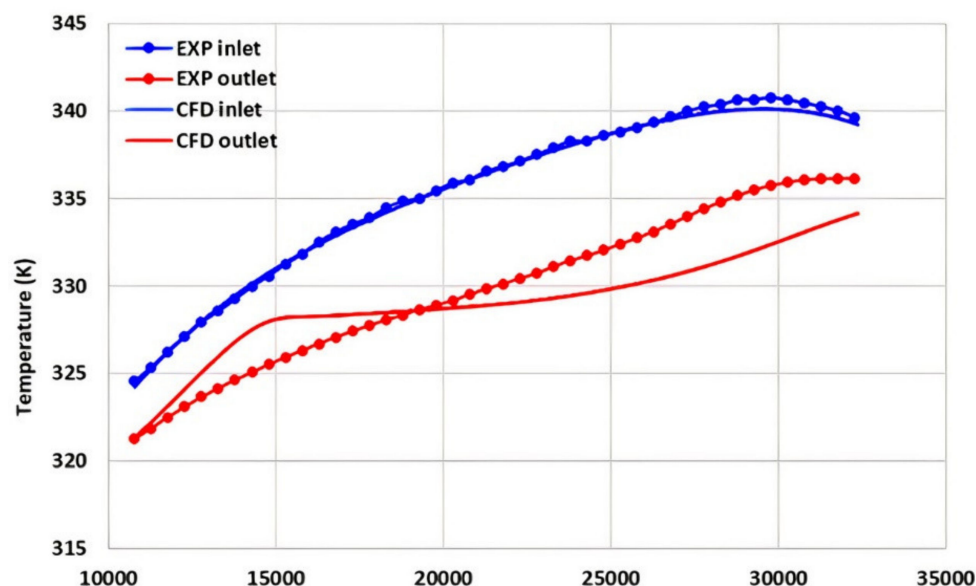


Figure 6. Water temperature comparison of CFD and experimental data.

The operation of the circulating pump was defined by an automated control unit, and for the validation only, a range of the system operation was examined, when the pump was continuously on. Water inlet and outlet temperatures were recorded (Figure 6). In the results of the CFD analysis, the phase change region was obviously shown by the plateau that formed around 54 °C. On the other hand, in the experimental results, the plateau was not clearly shown. This is mainly due to the fact that the CFD model is based on assumptions that are not considered in the experiment, as discussed in Section 3. In addition, there was good agreement on the stored energy value, where the experimental one was 3.73 kWh and the computational was 3.66 kWh. As the water temperature at the outlet and the stored energy were realistically predicted, it can be concluded that the CFD model can be used for further parametric studies of the system.

3.4. Conditions Studied

Three different HTF flow rates were studied in the closed loop charging circuit of the HEs, for each PCM. The flow rates studied were $0.007 \text{ kg}\cdot\text{s}^{-1}\cdot\text{m}^{-2}$, $0.01 \text{ kg}\cdot\text{s}^{-1}\cdot\text{m}^{-2}$, and $0.02 \text{ kg}\cdot\text{s}^{-1}\cdot\text{m}^{-2}$ according to EN ISO 9806 [40] and the surface area of the collector. Water was considered as the HTF, with a constant density of $998.2 \text{ kg}\cdot\text{m}^{-3}$ and all of its properties were provided by the software used [34].

Even the fastest charging flow was laminar, as it had a Reynolds (Re) number equal to 430 and this type of flow was modelled in the commercial CFD code. On the other hand, the slowest discharging flow was turbulent with $\text{Re} = 5330$, so all discharging flows were modelled using the standard $k-\epsilon$ turbulence model with default settings. This model can give reasonable accuracy in a range of turbulent flows and for this reason it is quite common. It has been validated as a model through the years and it has proven satisfactory performance in many applications.

The initial temperature of the whole computational domain, namely the phase change material, the tube, the fins, and the HTF, was set to 20 °C. This is an average ambient temperature for a sunny day, for Climatic Zone B in Greece [41]. HTF enters the HE at 70 °C, which is a typical temperature, expected at the outlet of the solar collector. The properties of the fins and tube materials were also provided by the simulation software [34]. The tank walls inside which the HE were immersed in the PCM are considered adiabatic, as in real applications, adequate insulation was used to minimize thermal losses. The charging process is considered to end when the PCM temperature was equal to 68 °C.

For the discharging circuit, the applied flow rates were equal to 480, 600, and 720 L·h⁻¹, which are the usual rates required by the regulations [40]. The inlet water temperature was equal to 15 °C, which is a typical supply water temperature for Climatic Zone B in Greece, for the cold months of the year [41]. The water temperature value was selected considering the worst-case scenario, for the discharging process. The initial temperature of the mesh computational domain for the discharging process was set at 65 °C, that is, 5 °C below the HTF inlet temperature of the charging circuit, considering again the worst case, where the system temperature decreased due to thermal losses.

4. Results

4.1. Charging Analysis of PCMs

In this section, typical results from the computational study for the three PCMs during the charging process, are presented and discussed. Tables A2 and A3 of the Appendix A show the numerical results concerning the duration of charging and the stored energy for each case examined. From a closer look at the tables, it is deduced that there is a tradeoff between fast charging and large storage capacity.

In particular, among the three PCMs studied, A53 and P53 required less time for charging than A58H, which is desirable, considering the short intervals when high intensity solar radiation is available during a day. Given the numbers, A53 requires 33–36% less time than A58H to reach 68 °C and this can be accomplished at approximately 4–7 h, contrary to A58H where the process may last as long as the impractical value of 11 h. From Table A2, it is also apparent that, as expected, the PCMs required less time for charging at higher values of HTF mass flow rates. Another general conclusion is that the size of the HE affects the charging duration. The larger the HE size, the more time is needed for a full charging, independently of the PCM type or the HTF flow rate, but this relationship is not linear as it will be discussed in the discharging section.

Considering the thermal capacity, the latent heat value is the PCM property with the greatest significance, and as a result, A58H application stored the largest energy amount, while A53 the least and P53 performed somewhere in between. A58H stored 10–16% more energy than A53. Of course, the larger the apparatus, the more stored energy, independently of the PCM type or the flow rate. However, in real applications of PCM storage tanks, a tradeoff between thermal losses to the ambient and heat transfer duration has been observed [27,33]. The more time is available for heat transfer between the HTF and the PCM tank, the higher the stored energy, provided that the slow charging does not suffer big thermal losses. On the contrary, the CFD simulation assumes fully adiabatic walls, so the stored energy does not depend on the HTF flow rate.

Figure 7 presents the area average temperature of PCM in the HE1 active PCM volume during charging, for all PCMs and all HTF flow rates. For the first 30 to 40 min, when most of the PCM did not change phase, the PCM temperature increased rapidly, due to sensible heat transfer mechanism. When the melting temperature was reached, the average temperature in the active PCMs volume increased but at a slower rate, due to latent heat. Regarding the dependence of the average PCM temperature with the HTF flow rate, it can be concluded that the PCM temperature over time increased with about the same rate in the first hour and then it was almost stabilized with a higher rate of increase for higher HTF flow rates, for all PCMs examined, as expected.

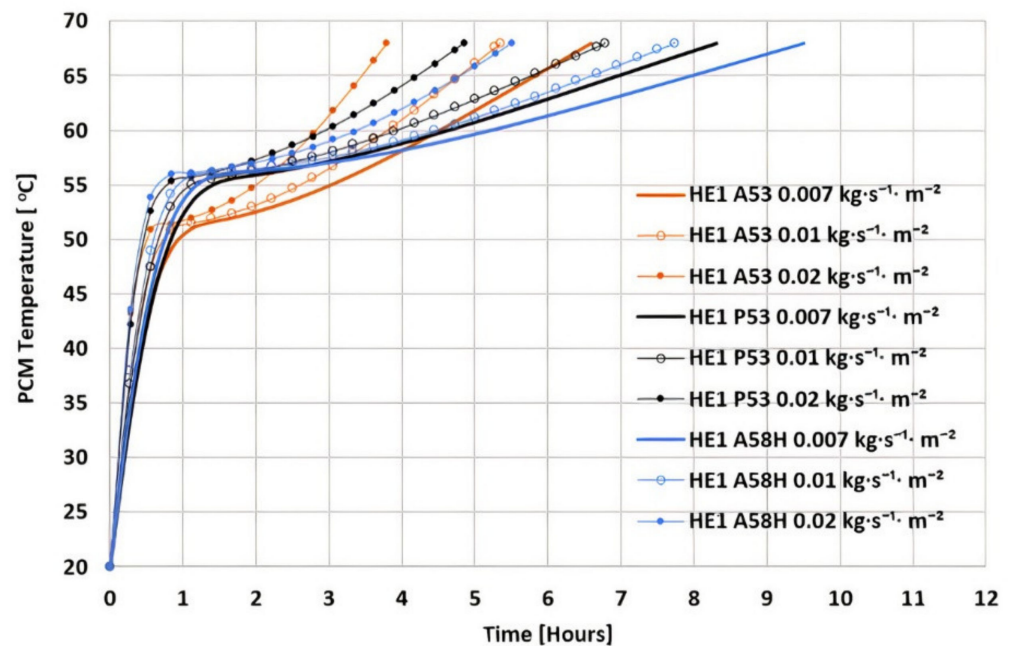


Figure 7. Area average temperature of PCM active volume during charging for all PCMs and all HTF flow rates studied, for HE1.

Figure 8 shows the stored energy during charging for all PCMs and all HTF flow rates for HE1. Independently of the flow rate, A53 stored energy faster than P53, which in turn stored faster than A58H. This is because of the increasing heat capacity, sensible and latent, of the three materials, but also their increasing melting temperatures. Considering the flow rate effect on the storing rate, it is obvious that the higher the flow rate, the higher the storing rate. The charging durations are listed in Table A2. The same conclusion was deduced by experimental results, both for charging and discharging [24].

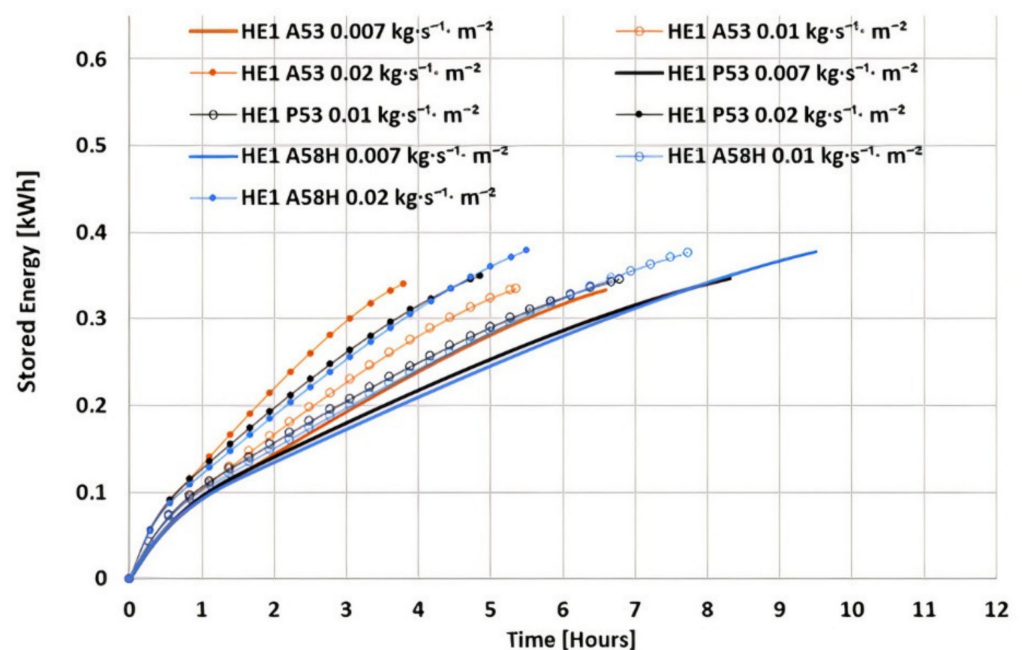


Figure 8. Stored energy during charging for all PCMs and all HTF flow rates, for HE1.

In addition, the accumulation rate of the resulting energy is fast at the beginning, where flushing of the cold water inside the tube takes place and the sensible heat transfer

mechanisms prevail. Then, the accumulation rate reduces for the biggest part of the charging duration and finally became even lower at the end, when the heat transfer rate was low. The same rate was evident in all charging and discharging cases that were experimentally investigated by [29]. Similarly, the progression of the liquid fraction with time during charging fits well with the numerical results of [16].

Figure 9 shows the area average temperature of PCM in the active PCM volume during charging, of all PCMs and all HTF flow rates, for HE2. Initially, the PCM temperature increased rapidly up to melting temperature. Then, the average PCM temperature increased at a very slow rate until PCM was fully charged and the average PCM temperature remained constant at 68 °C. From this Figure, it is also apparent that the rate of temperature increase is higher for higher HTF flow rates and it is higher for A53.

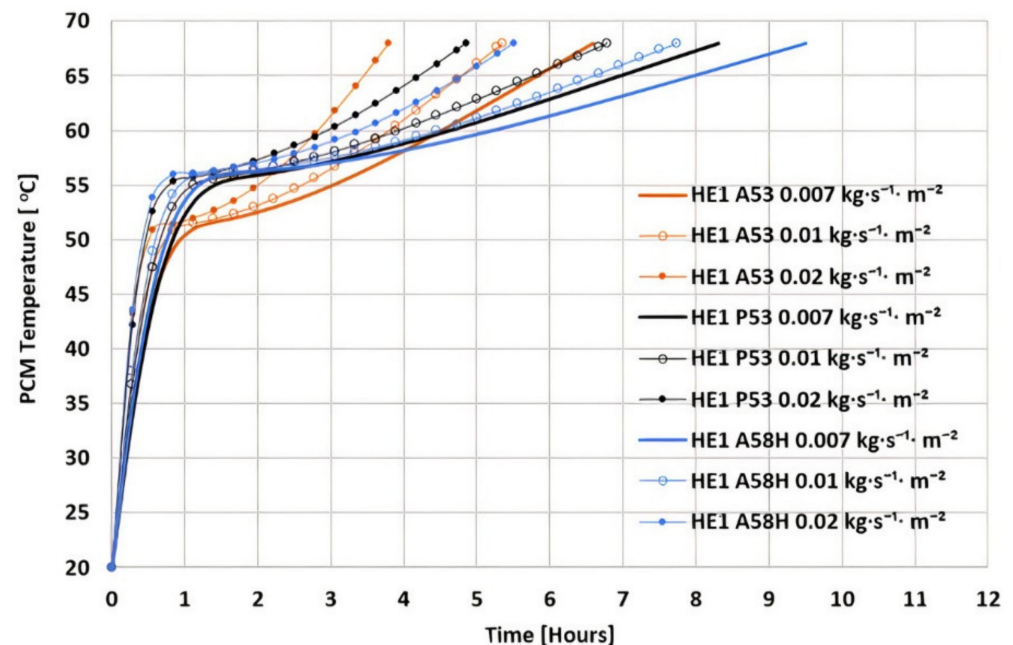


Figure 9. Area average temperature of PCM active volume during charging for all PCMs and all HTF flow rates studied, for HE2.

Figure 10 presents the stored energy per time for all PCMs and all HTF flow rates for HE2, respectively. It is apparent that more energy was stored for A58H and less for A53. In addition, P53 and A58H stored about the same amount of energy over time for the first hours and then A58H continued to store energy, while the stored energy in P53 remained constant, because it was fully charged. The behavior of A53 in HE2 was the same as in the HE1, i.e., it stored energy with the highest rate, but the total stored energy was less.

Figure 11 presents the results of area average temperature of PCM in the active PCM volume during charging, of all PCMs and all HTF flow rates studied for HE3. PCMs shows similar behavior as in the HEs examined before. A rapid increase of PCM temperature is noticed for the first hour, until melting temperature was reached. Subsequently, the average PCM temperature increased for most cases at a very slow rate until PCM was fully charged and the average PCM temperature remained constant. Temperature increase was higher for the HTF flow rate of $0.02 \text{ kg}\cdot\text{s}^{-1}\cdot\text{m}^{-2}$ and lower for HTF flow rate of $0.007 \text{ kg}\cdot\text{s}^{-1}\cdot\text{m}^{-2}$, as expected. A53 temperature increased with a higher rate, even in the latent heat region.

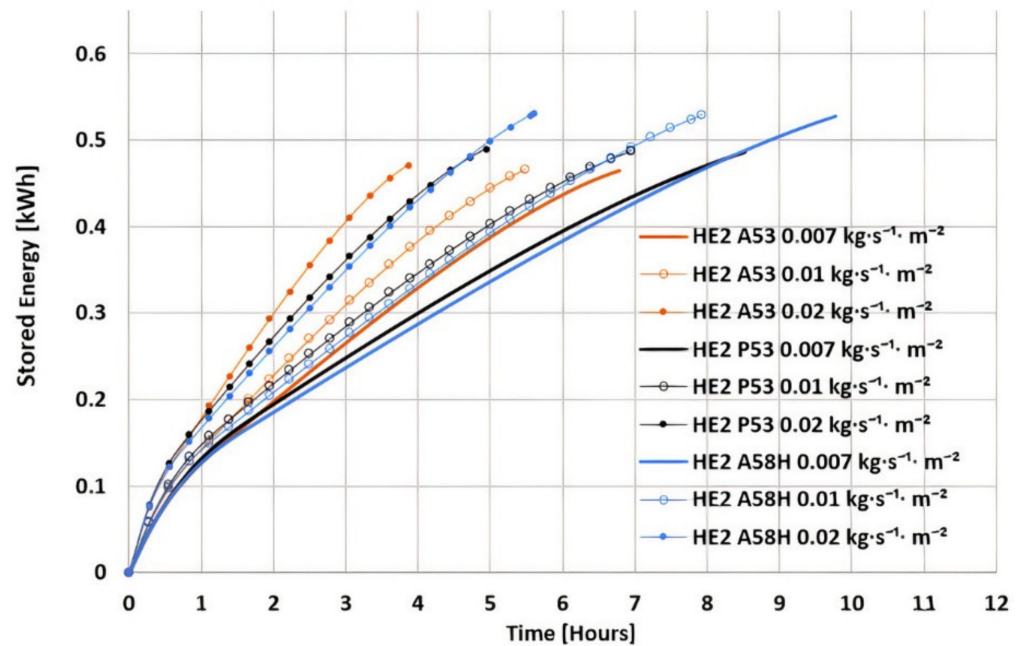


Figure 10. Stored energy during charging for all PCMs and all HTF flow rates studied, for HE2.

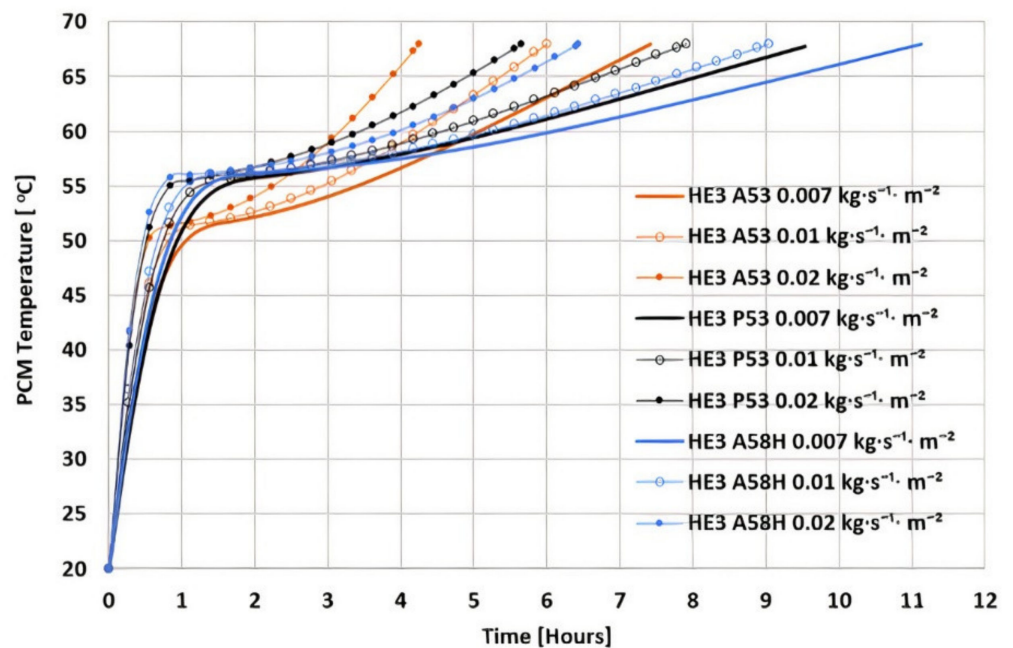


Figure 11. Area average temperature of PCM active volume during charging for all PCMs and all HTF flow rates, for HE3.

Charging was faster at higher HTF flow rates, as anticipated, but in contrast with the two smaller HEs, the behavior of A53 with the lowest and A58H with the highest HTF flow rate showed a slight difference. It is obvious that in HE3, A58H required more time for full charging at the HTF mass flow rate of $0.007 \text{ kg}\cdot\text{s}^{-1}\cdot\text{m}^{-2}$ and A53 at $0.02 \text{ kg}\cdot\text{s}^{-1}\cdot\text{m}^{-2}$ charged with the highest rate and at about two hours before P53, at the same HTF flow rate.

Figure 12 presents the stored energy during charging for all PCMs and all HTF flow rates for HE3. P53 and A58H were able to store about the same amount of energy as time passed, until P53 was fully charged. Then, A58H stored more energy until it was fully charged after some time. A53 stored less energy, but the rate of stored energy was higher.

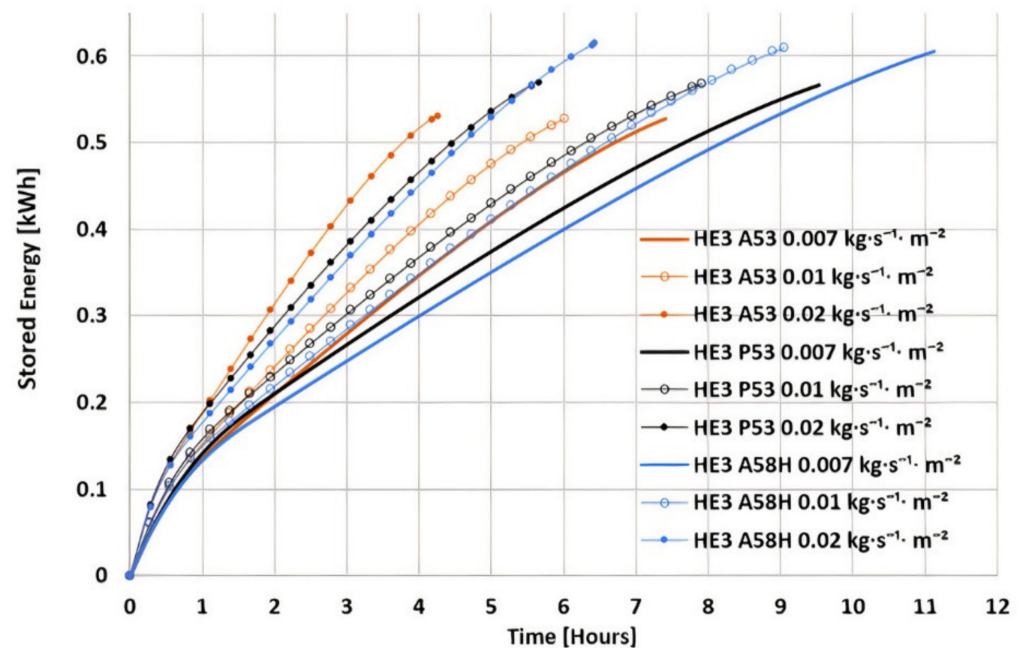


Figure 12. Stored energy during charging for all PCMs and all HTF flow rates studied, for HE3.

4.2. Discharging Analysis of PCMs

The next step of the computational study was the evaluation of the discharging circuit. The first regions where PCM solidification occurred were close to the tube and as time passed, PCM solidified close to the fins, as well. The efficiency of the system can be evaluated by calculating the duration for which the water temperature remains greater than 40 °C, which is the proposed temperature for domestic hot water usage. The mass flow rates for the discharging process were equal to 480, 600, and 720 L·h⁻¹, according to the regulations [40]. Figure 13 presents the water temperature at the outlet during the discharging process in HE1, for all PCMs studied, and the highest mass flow rate, i.e., the worst case. A58H provided hot water at temperatures higher than 40 °C for 12 min 4 s, P53 for 11 min 3 s, and A53 for 9 min 58 s. The PCM that gave a longer duration was A58H, although its full charging required up to 11 h. The calculated durations are satisfactory as they fall within the regulations.

Figure 14 illustrates the water outlet temperature as P53 discharged in three different HEs, for the worst case of mass flow rate, which was 720 L·h⁻¹. The water outlet temperature for HE1, HE2, and HE3 was greater than 40 °C for 11 min 3 s, 13 min 23 s, and 21 min 57 s, respectively. HE3 provided hot water for a longer duration, as was expected, since HE3 had the largest dimensions, thus the greater PCM volume.

Figure 15 depicts the effect of PCM volume on the duration of hot water production. This graph suggests that as the PCM volume increased, the duration increased also, but the rate of increase became higher for larger volumes, resulting in a nonlinear relationship between these two quantities. It is also clear that, for the same PCM volume, the duration increased as the flow rate decreased, but again in a nonlinear pattern. Therefore, considering the discharging process alone, it can be said that the large PCM volume or the slow flow rate have beneficial effects on the duration of hot water production, and doubling either the volume or the rate results in more than double the duration.

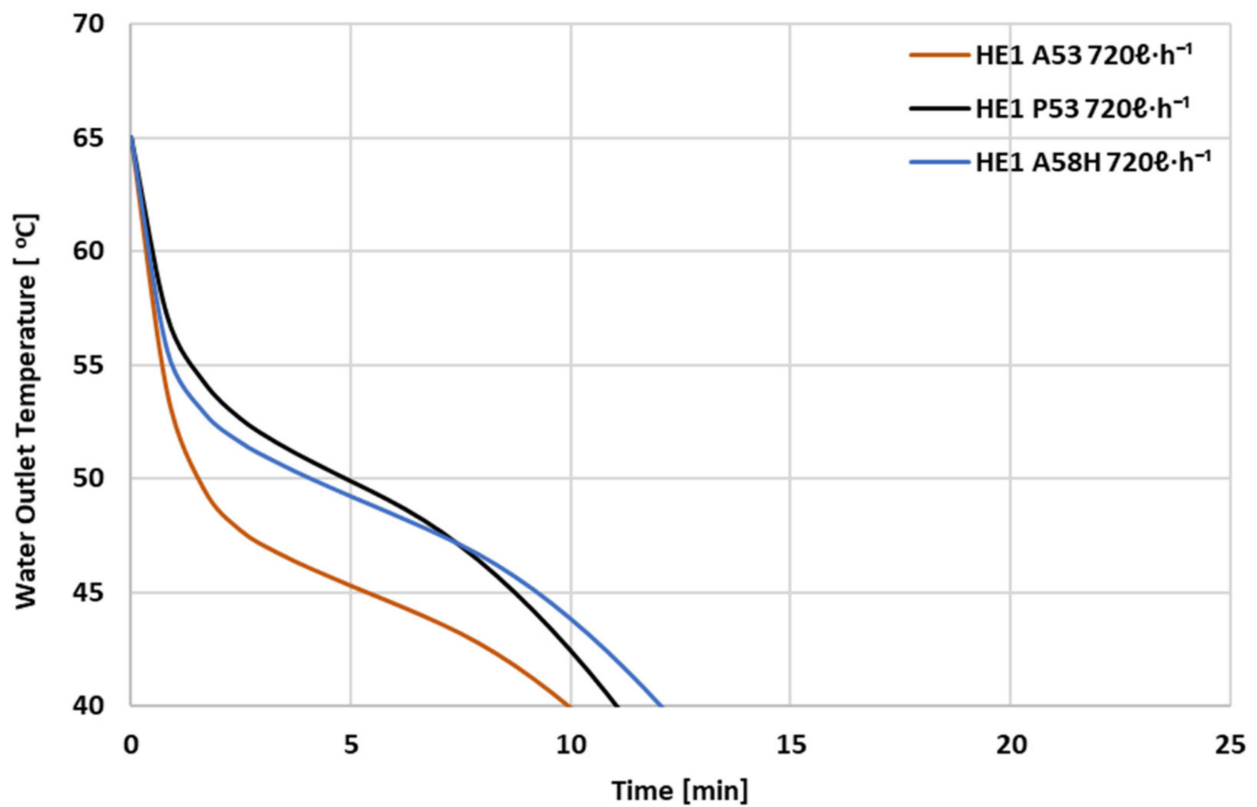


Figure 13. Water outlet temperature versus time for all PCMs studied, for HE1.

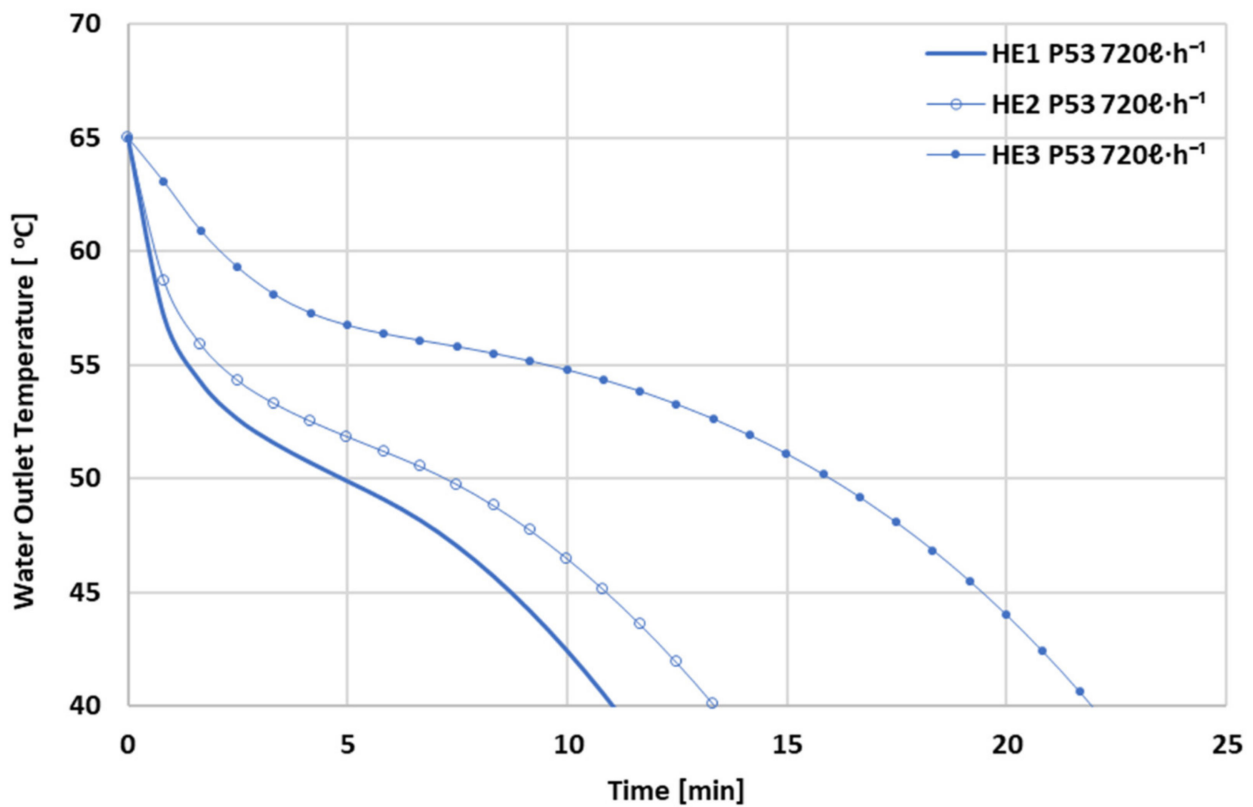


Figure 14. Water outlet temperature versus time for all HEs studied, for P53.

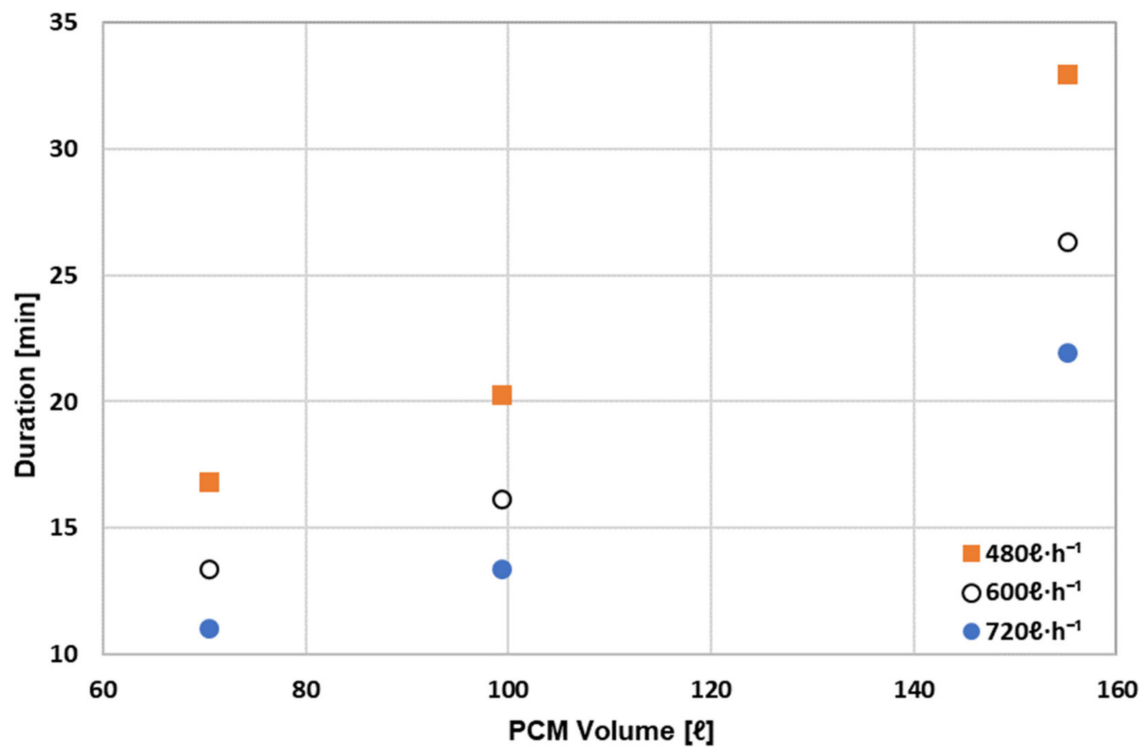


Figure 15. Duration of domestic hot water production versus PCM volume for P53 and three different mass flow rates.

Figure 16 shows the duration of DHW production for the smallest HE for three different flow rates, for P53. The lower flow rate provides hot water for 16 min 51 s, the medium for 13 min 23 s, and the highest for 11 min 8 s.

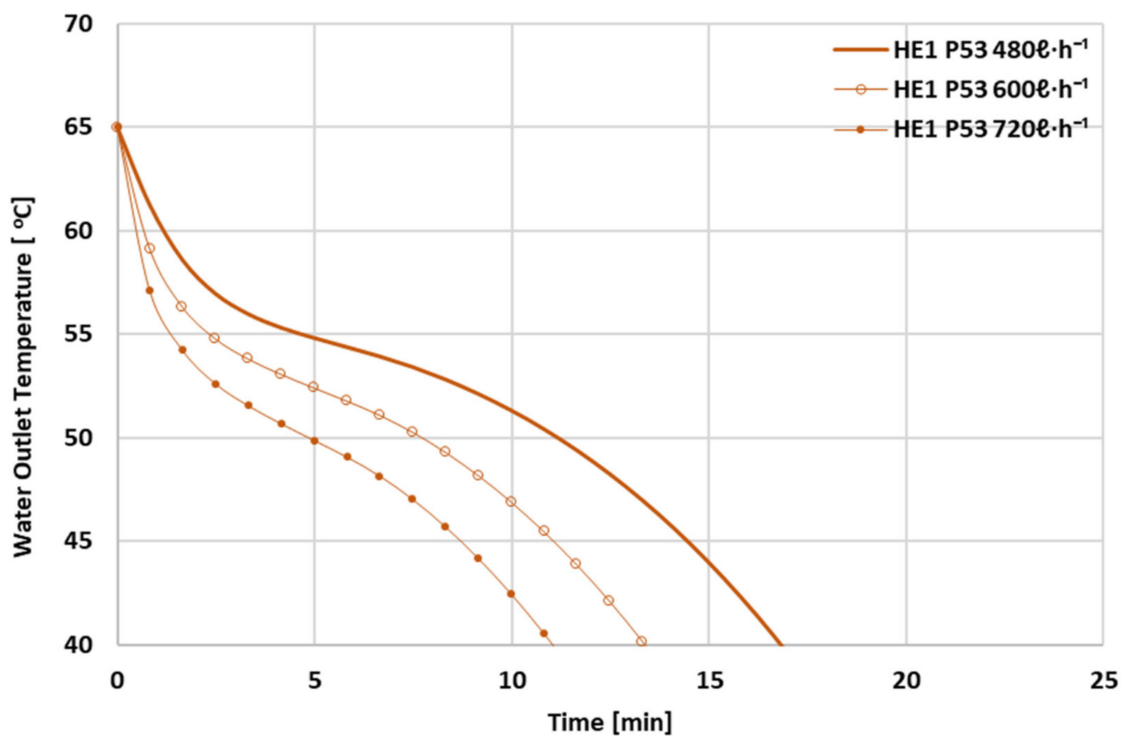


Figure 16. Water outlet temperature versus time for HE1, P53 and three different flow rates.

5. Conclusions

The thermal energy storage in a novel solar collector system, named Solar Kit, for DHW applications using PCM as storage material, was studied. The charging and discharging processes using different PCMs and flow rates and for different sizes of the tank and the HEs were computationally analyzed.

- The results of the numerical investigation for charging with PCMs A53, A58H, and P53 revealed that A53 and P53 required less time for charging, making them more suitable for PCM-integrated solar collectors. Moreover, the required duration for charging was decreased for higher HTF mass flow rates and Solar Kits of smaller dimensions. Concerning the stored heat amount, it was found to be independent of the HTF mass flow rate, since the walls of the tank were assumed to be adiabatic and it was greater for larger Solar Kits. The greatest heat amount was stored for A58H due to its higher latent heat value. The results of PCM area average temperature over time confirmed that the PCM temperature increased in the first hour rapidly and with about the same rate, and then the rate increased for higher HTF flow rates, regardless of the PCM.
- The charging duration using A58H was 1.4–1.5 times larger than A53 for all cases examined, but the energy that was stored during those periods was only 1.11–1.16 times more than A53. Similarly, the values for the paraffin P53 fell between these ranges. With a fast-charging PCM, a large thermal capacity could be achieved but not the largest. In a real application, thermal losses are expected to increase the duration and decrease the stored energy and their impact is stronger in long-lasting processes.
- The increase of HTF flow rate per square meter of collector from 0.007 to 0.020 kg·s⁻¹·m⁻² resulted in a decrease of the duration by about 0.57 times for all cases calculated. Assuming laminar flow, the increase of the flow rate strongly reduced the charging time for low rates and did not have a significant effect for higher rates. Considering the stored energy, because of the computational domain adiabatic walls, no change was observed, regardless of the flow rate.
- In addition, the gross collector area ratio between the medium and the small collector was 1.34 and between the large and the small was 1.93. The increase in duration between the medium and the small collector results were approximately 1.02 times for all PCMs and all flow rates. Similarly, the increase between the large and the small collector was between 1.12 and 1.17 times for all PCMs and all flow rates. Considering the stored energy, the increase was 1.4 times between the medium and the small collector and in the range of 2.23–2.34 times between the large and the small. So, the increase of the collector size did not significantly change the charging duration according to the computational model, but it beneficially changed the thermal capacity.
- The simulation of the discharging circuit for the worst conditions showed that all PCMs provide domestic hot water for satisfactory duration. Comparing the PCMs, A58H provided hot water for a longer duration. In general, the duration of hot water production was increased either by increasing the PCM volume, in other words the Solar Kit dimensions, or by decreasing the HTF mass flow rate. For the discharging process, using the small HE with the higher flow rate and A53 was the worst-case scenario. The amount of DHW having a temperature above 40 °C resulting from the computational model for the worst case was 119.6 L and the corresponding duration was 10 min. For the conditions tested, A58H resulted in a 1.21 times longer duration than A53, while P53 in 1.11 times longer than A53. The discharging duration for P53 and 720 L·h⁻¹ was increased by 1.2 times between the medium and the small collector and by 2.0 times between the large and the small. The relationship between the size of the collector and the duration was not linear, so doubling the size resulted in more than double the amount of DHW. Finally, the increase in the consumption flow rate reduced the duration, but again not linearly. For all cases examined, when the consumption rate was increased by 25% from low to medium and by 50% from low to high rate, the duration was reduced by 20% and 34%, respectively.

Author Contributions: Conceptualization, M.G.V., Y.G.C. and M.K.K.; methodology, M.G.V., Y.G.C., M.K.K. and P.P.; software, E.D., C.P. and G.D.; validation, E.D., C.P. and G.D.; formal analysis, E.D. and G.D.; investigation, all; writing—original draft preparation, M.K.K., E.D., G.D. and C.P.; writing—review and editing, M.K.K., E.D., G.D. and Y.G.C.; supervision, M.G.V. and Y.G.C.; project administration, M.G.V., Y.G.C. and M.K.K.; funding acquisition, M.G.V. and Y.G.C. All authors have read and agreed to the published version of the manuscript.

Funding: This research was funded by the Operational Programme Competitiveness, Entrepreneurship and Innovation, under the call RESEARCH—CREATIVE—INNOVATE, grant number T1 EDK—01898.

Conflicts of Interest: The authors declare no conflict of interest.

Appendix A

Mathematical Description of Charging and Discharging Processes

The two main mechanisms for storing energy in materials are sensible and latent heat storage [9]. In Solar Kit, LHS is mostly utilized for heat storage. The storage capacity of the latent system with a PCM medium can be calculated by Equation (A1) or Equation (A2) [2]:

$$Q = \int_{T_i}^{T_m} m \cdot c_{p,s} \cdot dT + m \cdot \beta \cdot \Delta h_m + \int_{T_m}^{T_f} m \cdot c_{p,l} \cdot dT \quad (\text{A1})$$

or

$$Q = m \cdot c_{p,s} \cdot (T_m - T_i) + m \cdot \beta \cdot \Delta h_m + m \cdot c_{p,l} \cdot (T_f - T_m), \quad (\text{A2})$$

where T_m is the melting temperature, T_i is the initial temperature, and T_f is the final temperature [K]; Q is the energy stored in the PCM [J], m is the PCM mass [kg], $c_{p,l}$ is the specific heat capacity of liquid PCM [$\text{J} \cdot \text{kg}^{-1} \cdot \text{K}^{-1}$], $c_{p,s}$ is the specific heat capacity of solid PCM [$\text{J} \cdot \text{kg}^{-1} \cdot \text{K}^{-1}$], β is the fraction of PCM melted, and Δh_m is the heat of fusion per mass unit [$\text{J} \cdot \text{kg}^{-1}$].

At first, the temperature of the PCM rose from the initial temperature, T_i , until it reached the melting temperature, T_m , via sensible heat storage. When the PCM reached the melting temperature and started melting, energy was stored via the latent heat of phase change. Lastly, when the entire PCM was melted, the medium raised its temperature until it reached the HTF temperature and again a small amount of energy was stored in the form of sensible heat, as initially. The most energy was stored during the intermediate phase.

The PCM phase change, conjugated to heat transfer by conduction in the tube wall and to the HTF forced convection, was unsteady. The mathematical model for the description of the heat transport phenomena relies on the following simplified assumptions: the PCM is homogeneous and isotropic; natural convection in the PCM is neglected; azimuthal temperature is everywhere negligible (2D solution). For the mathematical description of the solidification/melting process, the enthalpy–porosity technique [32–34] was commonly used. This technique was also used in commercial CFD codes as ANSYS® Fluent [34].

Fluent uses the Finite Volume Method to solve the fundamental conservation equations, with a cell-centered formulation, in a discretized domain. In Table A1 the main configurations of the numerical scheme are listed, as well the under-relaxation factors that were applied to achieve fast convergence of the solution. The time step of 1 s was selected, after a series of tests, as it is shown that this value can offer acceptable accuracy of the results in a plausible computational time.

Table A1. Numerical model details [34].

Solver Type		Pressure Based
Algorithm (Pressure–Velocity Coupling)		SIMPLE
Spatial Discretization	Gradient	Least Squares Cell Based
	Pressure	Second Order
	Density	Second Order Upwind
	Momentum	Second Order Upwind
	Energy	Second Order Upwind
Time Step Discretization		Second Order Implicit
Residuals	Continuity	1×10^{-3}
	X-velocity	1×10^{-3}
	Y-velocity	1×10^{-3}
	Z-velocity	1×10^{-3}
	Energy	1×10^{-6}
Time Step		1 s
Max Iterations per Time Step		250
Under-Relaxation Factors	Pressure	0.3
	Density	1
	Momentum	0.7
	Liquid Fraction Update	0.9
	Energy	1

For the calculation of the physical quantities that describe the laminar flow and the heat transfer between the HTF, the tube, the fins, and the PCM, the conservation equations of mass, momentum, and energy are solved by Fluent solver. The continuity equation was given by Equation (A3) [34]:

$$\frac{\partial \rho}{\partial t} + \nabla \cdot (\rho \cdot \vec{v}) = 0, \quad (\text{A3})$$

The first term describes how fast the density changes with time and the second term describes the flow of mass through the boundaries of a computational cell. The conservation of momentum is given by Equation (A4).

$$\frac{\partial (\rho \cdot \vec{v})}{\partial t} + \nabla \cdot (\rho \cdot \vec{v} \cdot \vec{v}) = -\nabla p + \nabla \cdot \left(\mu \left[\left(\nabla \vec{v} + \nabla \vec{v}^T \right) - \frac{2}{3} \cdot \nabla \cdot \vec{v} I \right] \right), \quad (\text{A4})$$

The first term at the left hand of Equation (A4) describes the rate of velocity increase and the second term is the convection rate. At the right-hand side, the first term describes the pressure gradient effect and the second term is the divergence of the stress tensor, where μ is the molecular viscosity and I the unit tensor. The term I describes the effect of volume dilatation. The energy equation is given by Equation (A5):

$$\frac{\partial (\rho \cdot E)}{\partial t} + \nabla \cdot \left(\vec{v} \cdot (\rho \cdot E + p) \right) = \nabla \cdot (k \cdot \nabla T) + S, \quad (\text{A5})$$

The first term on the right hand of Equation (A5) represents the heat transfer by conduction and the second term is added to account for a pressure drop according to the Carman–Kozeny law of the enthalpy–porosity approach. The enthalpy in Equation (A6) is given by Equation (A7), where T_{ref} is maintained to the default value of 298.15 K.

$$E = h - \frac{p}{\rho} + \frac{\vec{v}^2}{2}, \quad (\text{A6})$$

$$h = \int_{T_{ref}}^T c_p \cdot dT, \quad (A7)$$

where ρ is the mass density [$\text{kg}\cdot\text{m}^{-3}$], t the time [s], \vec{v} the velocity vector [$\text{m}\cdot\text{s}^{-1}$], p the pressure [Pa], k the thermal conductivity [$\text{W}\cdot\text{m}^{-1}\cdot\text{K}^{-1}$], and h is the specific enthalpy [$\text{J}\cdot\text{kg}^{-1}$]. Heat transfer in solids (tube and fins) is described by the energy equation given by Equation (A8).

$$\frac{\partial(\rho \cdot h)}{\partial t} = \nabla \cdot (k \cdot \nabla T), \quad (A8)$$

Table A2. Time for charging of A53, P53, and A58H for three different HTF mass flow rates for each selected HE.

	HTF Mass Flow Rate ($\text{kg}\cdot\text{s}^{-1}\cdot\text{m}^{-2}$)	Time for PCM Charging (Hours)		
		A53	P53	A58H
Heat Exchanger 1	0.007	6.60	8.31	9.51
	0.010	5.35	6.79	7.73
	0.020	3.79	4.85	5.50
Heat Exchanger 2	0.007	6.78	8.53	9.77
	0.010	5.49	6.95	7.93
	0.020	3.86	4.95	5.61
Heat Exchanger 3	0.007	7.41	9.54	11.13
	0.010	6.01	7.92	9.05
	0.020	4.25	5.65	6.43

In the enthalpy–porosity method [32–34], the melting interface is not tracked explicitly. Instead, a quantity called the liquid fraction, which indicates the fraction of the cell volume that is in liquid form, is associated with each cell in the domain. The liquid fraction is computed at each iteration, based on an enthalpy balance. Moreover, the temperature below which the PCM is completely solid is called the solidus temperature and the temperature above which the PCM is completely liquid is the liquidus temperature. The mushy zone, namely the region in which the liquid fraction lies between 0 and 1, is modeled as a “pseudo” porous medium, in which the porosity decreases from 1 to 0 as the material solidifies. When the material is fully solidified in a cell, the porosity becomes zero and hence the velocities also drop to zero. For the energy equation, the enthalpy of the material is computed as the sum of the sensible enthalpy and the latent heat.

Table A3. Stored energy in A53, P53, and A58H for three different HTF mass flow rates and for each HE selected.

	HTF Mass Flow Rate ($\text{kg}\cdot\text{s}^{-1}\cdot\text{m}^{-2}$)	Stored Energy per Tube (kWh)			Total Stored Energy (kWh)		
		A53	P53	A58H	A53	P53	A58H
Heat Exchanger 1	0.007	0.333	0.347	0.370	4.662	4.858	5.180
	0.010	0.335	0.346	0.376	4.690	4.844	5.264
	0.020	0.340	0.350	0.379	4.760	4.900	5.306
Heat Exchanger 2	0.007	0.465	0.486	0.528	6.510	6.804	7.392
	0.010	0.466	0.488	0.529	6.524	6.832	7.406
	0.020	0.471	0.490	0.531	6.594	6.860	7.434
Heat Exchanger 3	0.007	0.527	0.566	0.605	10.540	11.320	12.100
	0.010	0.527	0.568	0.610	10.540	11.360	12.200
	0.020	0.531	0.570	0.615	10.620	11.400	12.300

References

1. Pagkalos, C.; Dogkas, G.; Koukou, M.; Konstantaras, J.; Lymperis, K.; Vrachopoulos, M. Evaluation of Water and Paraffin PCM as Storage Media for use in Thermal Energy Storage Applications: A Numerical Approach. *Int. J. Thermofluids* **2020**, *1*, 100006. [CrossRef]
2. Heinz, A.; Schranzhofer, H. Thermal Energy Storage with Phase Change Materials—A Promising Solution? In Proceedings of the EuroSun 2010, Graz, Austria, 28 September–1 October 2010. [CrossRef]
3. Elias, C.; Stathopoulos, V. A comprehensive review of recent advances in materials aspects of phase change materials in thermal energy storage. *Energy Procedia* **2019**, *161*, 385–394. [CrossRef]
4. Demirbas, M. Thermal Energy Storage and Phase Change Materials: An Overview. *Energy Sources Part B Econ. Plan. Policy* **2006**, *1*, 85–95. [CrossRef]
5. Lizana, J.; Chargartegui, R.; Barrios-Padura, A.; Ortiz, C. Advanced low-carbon energy measures based on thermal energy storage in buildings: A review. *Renew. Sustain. Energy Rev.* **2018**, *82*, 3705–3749. [CrossRef]
6. Nkwetta, D.; Haghighat, F. Thermal energy storage with phase change materials. A state-of-the art review. *Sustain. Cities Soc.* **2014**, *10*, 87–100. [CrossRef]
7. Mehling, H.; Cabeza, L. *Heat and Cold Storage with PCM—An Up to Date Introduction into Basics and Applications*, 1st ed.; Springer-Verlag: Berlin/Heidelberg, Germany, 2008. [CrossRef]
8. Koukou, M.; Vrachopoulos, M.; Tachos, N.; Dogkas, G.; Lymperis, K.; Stathopoulos, V. Experimental and Computational Investigation of a Latent Heat Energy Storage System with a Staggered Heat Exchanger for Various Phase Change Materials. *Therm. Sci. Eng. Prog.* **2018**, *7*, 87–98. [CrossRef]
9. Palomba, V.; Frazzica, A. Comparative analysis of thermal energy storage technologies through the definition of suitable key performance indicators. *Energy Build.* **2019**, *185*, 88–102. [CrossRef]
10. Tesse2b PROJECT DELIVERABLE 8.5: Training MATERIAL. Available online: http://www.tesse2b.eu/Content/images/tesse2b/Training_Material.pdf (accessed on 6 July 2021).
11. Mohamed, S.; Al-Sulaiman, F.; Ibrahim, N.; Zahir, M.; Al-Ahmed, A.; Saidur, R.; Yilbaş, B.; Sahin, A. A review on current status and challenges of inorganic phase change materials for thermal energy storage systems. *Renew. Sustain. Energy Rev.* **2016**, *70*, 1072–1089. [CrossRef]
12. Salunkhe, P.; Jaya Krishna, D. Investigations on latent heat storage materials for solar water and space heating applications. *J. Energy Storage* **2017**, *12*, 243–260. [CrossRef]
13. Pielichowska, K.; Pielichowski, K. Phase change materials for thermal energy storage. *Prog. Mater. Sci.* **2014**, *65*, 67–123. [CrossRef]
14. Abokersh, M.; Osman, M.; Elbaz, O.; El-Morsi, M.; Sharaf, O. Review of the phase change material (PCM) usage for solar domestic water heating systems (SDWHS). *Int. J. Energy Res.* **2017**, *41*, 329–357. [CrossRef]
15. Nallusamy, N.; Sampath, S.; Velraj, R. Experimental investigation on a combined sensible and latent heat storage system integrated with constant/varying (solar) heat sources. *Renew. Energy* **2007**, *32*, 1206–1227. [CrossRef]
16. El Qarnia, H. Numerical analysis of a coupled solar collector latent heat storage unit using various phase change materials for heating the water. *Energy Convers. Manag.* **2009**, *50*, 247–254. [CrossRef]
17. Reddy, R.; Nallusamy, N.; Reddy, K.H. Experimental studies on phase change material-based thermal energy storage system for solar water heating applications. *J. Fundam. Renew. Energy Appl.* **2012**, *2*, R120314. [CrossRef]
18. Cabeza, L.; Nogues, M.; Roca, J.; Illa, J.; Hiebler, S.; Mehling, H. PCM-module to improve hot water heat stores with stratification: First tests in a complete solar system. In Proceedings of the Ninth International Conference on Thermal Energy Storage, Warsaw, Poland, 1–4 September 2003.
19. Mazman, M.; Cabeza, L.; Mehling, H.; Nogues, M.; Evliya, H.; Paksoy, H. Utilization of phase change materials in solar domestic hot water systems. *Renew. Energy* **2009**, *34*, 1639–1643. [CrossRef]
20. Malvi, C.; Gupta, A.; Gaur, M.; Crook, R.; Dixon-Hardy, D. Experimental Investigation of Heat Removal Factor in Solar Flat Plate Collector for Various Flow Configurations. *Int. J. Green Energy* **2017**, *14*, 442–448. [CrossRef]
21. Kaygusuz, K. Experimental and theoretical investigation of latent heat storage for water based solar heating systems. *Energy Convers. Manag.* **1995**, *36*, 315–323. [CrossRef]
22. Abdulateef, A.; Mat, S.; Abdulateef, J.; Sopian, K.; Al-Abidi, A. Geometric and design parameters of fins employed for enhancing thermal energy storage systems: A review. *Renew. Sustain. Energy Rev.* **2018**, *82*, 1620–1635. [CrossRef]
23. Dhaidan, N.; Khodadadi, J. Improved performance of latent heat energy storage systems utilizing high thermal conductivity fins: A review. *J. Renew. Sustain. Energy* **2017**, *9*, 034103. [CrossRef]
24. Khan, I.; Khan, M.I. Experimental Study of Mass Flow Rates of HTF on PCM Based Solar Thermal Energy Storage. *VW Eng. Int.* **2021**, *3*, 23–28.
25. Qureshi, Z.; Ali, H.; Khushnood, S. Recent advances on thermal conductivity enhancement of phase change materials for energy storage system: A review. *Int. J. Heat Mass Transf.* **2018**, *127*, 838–856. [CrossRef]
26. Lin, Y.; Jia, Y.; Alva, G.; Fang, G. Review on thermal conductivity enhancement, thermal properties and applications of phase change materials in thermal energy storage. *Renew. Sustain. Energy Rev.* **2018**, *82*, 2730–2742. [CrossRef]
27. Naghavi, M.; Ang, B.; Rahmanian, B.; Naghavi, S.; Bazri, S.; Mahmoodian, R.; Metselaar, H. On-Demand Dynamic Performance of a Thermal Battery in Tankless Domestic Solar Water Heating in the Tropical Region. *Appl. Therm. Eng.* **2020**, *167*, 114790. [CrossRef]

28. Kilickap, S.; El, E.; Yildiz, C. Investigation of the Effect on the Efficiency of Phase Change Material Placed in Solar Collector Tank. *Therm. Sci. Eng. Prog.* **2018**, *5*, 25–31. [[CrossRef](#)]
29. Fadl, M.; Eames, P. Thermal Performance Analysis of the Charging/Discharging Process of a Shell and Horizontally Oriented Multi-Tube Latent Storage System. *Energies* **2020**, *13*, 6193. [[CrossRef](#)]
30. DIMAS SA. Dimas Solar Thermal Industry. Available online: <https://dimas-solar.gr/> (accessed on 31 May 2020).
31. Medrano, M.; Yilmaz, M.; Nogues, M.; Martorell, I.; Roca, J.; Cabeza, L. Experimental Evaluation of Commercial Heat Exchangers for use as PCM Thermal Storage Systems. *Appl. Energy* **2009**, *86*, 2047–2055. [[CrossRef](#)]
32. Koukou, M.; Dogkas, G.; Vrachopoulos, M.; Konstantaras, J.; Pagkalos, C.; Stathopoulos, V.; Pandis, P.; Lymperis, K.; Coelho, L.; Rebola, A. Experimental assessment of a full scale prototype thermal energy storage tank using paraffin for space heating application. *Int. J. Thermofluids* **2020**, *1–2*, 100003. [[CrossRef](#)]
33. Dogkas, G.; Konstantaras, J.; Koukou, M.; Vrachopoulos, M.; Pagkalos, C.; Stathopoulos, V.; Pandis, P.; Lymperis, K.; Coelho, L.; Rebola, A. Development and experimental testing of a compact thermal energy storage tank using paraffin targeting domestic hot water production needs. *Therm. Sci. Eng. Prog.* **2020**, *19*, 100573. [[CrossRef](#)]
34. ANSYS®. *Academic Research, Release 18.0*; ANSYS, Inc.: Canonsburg, PA, USA, 2017.
35. Vidi, S.; Mehling, H.; Hemberger, F.; Hausmann, T.; Laube, A. Round-Robin Test of Paraffin Phase-Change Material. *Int. J. Thermophys.* **2014**, *36*, 2518–2522. [[CrossRef](#)]
36. Mehling, H.; Barreneche, C.; Sole, A.; Cabeza, L. The Connection Between the Heat Storage Capability of PCM as a Material Property and their Performance in Real Scale Applications. *J. Energy Storage* **2017**, *13*, 35–39. [[CrossRef](#)]
37. Mehling, H.; Ebert, H.; Schossig, P. Development of Standards for Materials Testing and Quality Control of PCM. In Proceedings of the 7th IIR Conference on Phase Change Materials and Slurries for Refrigeration and Air Conditioning, Dinan, France, 13–15 September 2006.
38. PCM Products Ltd. Phase Change Material Products Limited. Available online: <http://www.pcmproducts.net/files/A%20range-2018.pdf> (accessed on 15 March 2019).
39. Evangelakis, G.; Lagaris, I.; Papageorgiou, D.G.; Prouskas, K.; Zisopoulou, A.E. A Hybrid Numerical-Experimental Method for Determining Thermal Conductivities. *J. Heat Transf.* **2021**, *143*, 011702. [[CrossRef](#)]
40. *ELOT EN ISO 9806*; Solar Energy—Thermal Solar Collectors—Test Methods. ISO: Geneva, Switzerland, 2014.
41. Technical Chamber of Greece. *TOTEE 20701-3/2010. Climate Data of Greek Regions*; Technical Chamber of Greece: Athens, Greece, 2010.